NeuroImage 317 (2025) 121324

Contents lists available at ScienceDirect

NeuroImage

journal homepage: www.elsevier.com/locate/ynimg

Diffusion Bubble Model: A novel MRI approach for detection and subtyping of neonatal punctate white matter lesions

Erjun Zhang [a,b,c], Benjamin De Leener [a,b,c,d,*,1], Gregory A. Lodygensky [b,e,f,**,1]

[a] Institute of Biomedical Engineering, Polytechnique Montreal, Montreal, H3T 1J4, Quebec, Canada
[b] CHU Sainte-Justine Research Center, University of Montreal, Montreal, H3T 1C5, Quebec, Canada
[c] NeuroPoly Lab, Polytechnique Montreal, Montreal, H3T 1J4, Quebec, Canada
[d] Department of Computer Engineering and Software Engineering, Polytechnique Montreal, Montreal, H3T 1J4, Quebec, Canada
[e] Department of Pediatrics, University of Montreal, Montreal, H3T 1J4, Quebec, Canada
[f] Department of Pharmacology and Physiology, University of Montreal, Montreal, H3T 1J4, Quebec, Canada

ARTICLE INFO

Dataset link: link

Keywords:
Punctate white matter lesions
Diffusion bubble model
DBM
Diffusion MRI model
Neonatal brain injury
PWML
Isotropic diffusion spectrum

ABSTRACT

Diffusion magnetic resonance imaging, particularly diffusion tensor imaging (DTI), is an indispensable non-invasive tool for visualizing brain structure and detecting injuries by tracking water molecule motion. However, DTI may overlook subtle microstructural alterations due to its oversimplified model. In this study, we introduced the Diffusion Bubble Model (DBM), a spectrum-based framework that decomposes each voxel's signal into a continuum of isotropic "bubbles" after the anisotropic tensor adjustment, thereby capturing a spectrum with continuous range of restriction levels. From the resulting isotropic-diffusion spectrum we derive metrics representing the spectrum and free-water of the tissue voxel. We applied DBM to diffusion data from 20 infants with punctate white-matter lesions (PWMLs) in the optic radiation and compared lesion regions with contralateral regions as well as matched controls. DBM segregated the lesions into two phenotypes that DTI could not differentiate: wet-type (N = 10), showing up to +155.0% elevated free water versus control (+125.1% *vs.* contralateral), and dry-type (N = 10), with −68.4% less free water compared to contralateral and no difference versus controls. Notably, wet-type lesions exhibited stronger slow-diffusion shifts on DBM (−37.6% in the 1/4 area line, −52.7% in left FWHM) than changes in mean diffusivity (−30.3%) from DTI. These findings suggest that DBM can reveal microstructural heterogeneity invisible to conventional DTI, offering a promising tool for refined characterization and monitoring of neonatal brain injury.

1. Introduction

Magnetic Resonance Imaging (MRI), developed in the 1970s, has become an indispensable, non-invasive tool for visualizing brain structure, monitoring development, and detecting injury (Lerch et al., 2017; Dubois et al., 2021; Alexander et al., 2007). Among various MRI techniques, diffusion MRI (dMRI), introduced in the 1980s, has gained prominence for its ability to probe tissue homeostasis and microstructure by sensitizing the signal to the motion of water molecules (Merboldt et al., 1985; Pierpaoli et al., 1996). By providing insights into the cellular milieu, dMRI offers valuable information for both clinical applications and neuroscientific research (Jelescu and Budde, 2017; Merboldt et al., 1985; Pierpaoli et al., 1996; Le Bihan et al., 2001).

Diffusion Tensor Imaging (DTI), a simple yet foundational dMRI model, represents water diffusion as a 3D ellipsoid tensor and allows for the characterization of brain microstructure (Jelescu and Budde, 2017). DTI-derived metrics capture distinct aspects of this diffusion: axial diffusivity (AD) quantifies diffusion along dominant fiber orientations; radial diffusivity (RD) measures diffusion perpendicular to these orientations; mean diffusivity (MD) reflects the overall magnitude of water diffusion; and fractional anisotropy (FA) captures the directional preference of the diffusion (Le Bihan et al., 2001; Alexander et al., 2007; Pavaine et al., 2016; Kersbergen et al., 2014). Changes in these metrics can indicate underlying microstructural alterations, such as

* Correspondence to: Department of Computer Engineering and Software Engineering, Polytechnique Montreal, L5618-2900 Edouard Montpetit Blvd, Montreal, H3T 1J4, Quebec, Canada.
** Correspondence to: CHU Sainte-Justine Research Center, Department of Pediatrics, 3175 Chemin Cote Sainte-Catherine, Montreal, H3T 1C5, Quebec, Canada.
E-mail addresses: erjun.zhang@hotmail.com (E. Zhang), benjamin.de-leener@polymtl.ca (B. De Leener), ga.lodygensky@umontreal.ca (G.A. Lodygensky).
[1] These authors contributed equally as co-corresponding authors.

https://doi.org/10.1016/j.neuroimage.2025.121324
Received 15 February 2025; Received in revised form 15 May 2025; Accepted 11 June 2025
Available online 25 June 2025

demyelination (elevated RD) and axonal damage (reduced AD) (Winklewski et al., 2018; Sun et al., 2006; Song et al., 2002; Alexander et al., 2007).

Despite its simplicity and widespread use, DTI has notable limitations. Its single-tensor model cannot fully capture the complexity of the tissue microstructure within each voxel, and it only provides averaged diffusion information (Lerch et al., 2017; Jelescu et al., 2020). This shortcoming becomes particularly evident in conditions with mixed pathology, where multiple compartments (e.g., demyelinated axons, inflammatory cells, altered extracellular space) or axon bundles with different orientations contribute to the diffusion signal (Cross and Song, 2017; DiPiero et al., 2022). The partial volume effect and other confounding factors may further obscure subtle changes, making it challenging to pinpoint the underlying pathology (Jeon et al., 2018; Henf et al., 2018).

To overcome these limitations, biophysical multi-compartment models partition the signal into a few predefined pools, typically intra-axonal, extra-axonal and free water, and estimate their respective volume fractions and diffusivity (Niendorf et al., 1996; Alexander et al., 2007). Representative examples include the free water elimination (FWE) model, neurite orientation dispersion and density imaging (NODDI) and soma and neurite density imaging (SANDI) (White et al., 2013; Zhang et al., 2012; Palombo et al., 2020). While biologically intuitive, these models assume that just a few discrete compartments can represent the underlying microstructural heterogeneity. In reality, tissue diffusivity spans a continuum, producing a broad spectrum of apparent diffusion coefficients (Yablonskiy et al., 2003).

Spectrum-based approaches attempt to embrace this continuum. Diffusion spectrum imaging (DSI) directly reconstructs the full probability density function of the diffusion displacement by sampling in the three-dimensional q-space. Diffusion basis spectrum imaging (DBSI) and restriction spectrum imaging (RSI) fit the data with a series of components spanning a range of diffusivity or spatial scales (Wang et al., 2011; White et al., 2013). DSI, however, demands hundreds of directions, whereas DBSI and RSI usually exploit only part of the recovered spectrum in subsequent biological interpretation.

Building on these landmark articles, we introduce the Diffusion Bubble Model (DBM), a simple, stable and spectrum-based approach to analyzing brain microstructure with dMRI. The model represents the voxel signal as the superposition of numerous mono-exponential decays ("bubbles") with purely isotropic diffusion tensors. Fitting this continuous isotropic spectrum generates a compact "fingerprint" of the local restriction landscape without prescribing how many compartments exist or what their diffusivity should be. Directional information, when needed, can be retained through a small set of averaged anisotropic tensors, but is not required for spectrum estimation. Among the open-source models, FWE provides a well-validated estimation of the fast (free-water) compartment, precisely the high-diffusivity tail that appears in the DBM spectrum. Comparing the DBM's fast-diffusion coefficient with the FWE free-water fraction therefore offers an independent cross-check that the spectrum is biologically meaningful. DTI, meanwhile, remains the clinical workhorse and offers a familiar baseline against which to gauge any added value. We tested DBM in in-vivo neonatal data containing punctate white-matter lesions (PWMLs), a common injury in neonates, that can be associated with long-term motor, cognitive, and behavioral deficits (de Bruijn et al., 2023; Tusor et al., 2017; Guo et al., 2017; de Bruïne et al., 2011; Arberet et al., 2017). PWMLs typically appear hyperintense on T1-weighted (T1w) images and hypointense on T2-weighted (T2w) images, and restricted diffusion on diffusion maps, though they can sometimes present with only subtle or even no detectable T2w and DTI-based changes (Nguyen et al., 2019; Pavaine et al., 2016; Niwa et al., 2011; Rutherford et al., 2010; Hayman et al., 2019).

We hypothesize that DBM will detect PWML-related microstructural alterations more sensitively than DTI and will match the FWE model's ability to isolate fast (free-water) signal. Specifically, we anticipate a leftward (toward lower diffusivities) shift in the isotropic spectrum within PWML regions, consistent with increased restriction. By comparing DBM-derived metrics with both DTI parameters and the FWE free-water fraction, we aim to establish DBM as a simple, robust, clinically practical tool for identifying PWMLs and characterizing their underlying tissue damage.

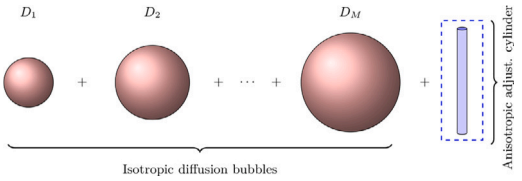

Fig. 1. Schematic illustration of the Diffusion Bubble Model (DBM). Red balls represent isotropic diffusion "bubbles" of varying sizes, each corresponding to a distinct isotropic diffusion tensor. The blue cylinder is the anisotropic adjustment term, capturing the apparent anisotropic diffusion effects along specific directions (only a single cylinder is shown here for simplicity). By decomposing the measured signal into these isotropic and anisotropic adjustment terms, DBM provides a more comprehensive representation of tissue microstructure than conventional diffusion tensor models.

2. Methods

2.1. Model

The Diffusion Bubble Model assumes that the measured diffusion-weighted signal can be decomposed into a combination of isotropic components and averaged anisotropic contributions. First, the model separates the apparent anisotropic contribution (anisotropic adjustment term) from the diffusion signal, thereby enabling a clearer characterization of the isotropic diffusion elements that remain. These isotropic components are then represented as a continuous spectrum of isotropic diffusion "bubbles", each corresponding to an isotropic diffusion tensor with a distinct effective radius or diffusion scales.

A schematic representation of DBM is provided in Fig. 1. Here, the red balls correspond to isotropic diffusion tensors ("bubbles"), while the blue cylinder(s) represent anisotropic adjustment diffusion tensors aligned along specific direction(s). By decomposing the diffusion MRI signal into these elements, DBM aims to provide a more detailed and sensitive representation of the underlying tissue microstructure than conventional diffusion tensor models. Fig. 2 illustrates DBM generates an isotropic diffusion spectrum/coefficient curve by plotting the isotropic diffusion "bubble" decomposition coefficients against increasing isotropic "bubble" diameters. This curve provides a detailed profile of the isotropic diffusion distribution within the tissue. We hypothesize that for tissues affected by a pathology (punctate white matter lesions in this study), the isotropic diffusion spectrum curve may shift, indicating altered microstructural properties compared to healthy control tissues. Through this decomposition, DBM may detect subtle tissue changes more sensitively than traditional diffusion models.

$$S_k/S_0 = \sum_{i=1}^{M} f_{D_i} e^{-b_k \mathbf{g_k}^T \mathbf{D_i} \mathbf{g_k}} + \sum_{j=1}^{N} f_{D_j} e^{-b_k \mathbf{g_k}^T \mathbf{D_j} \mathbf{g_k}} + \epsilon_k \quad (1)$$

$$S_k/S_0 = S_{iso} + S_{aniso} + \epsilon_k \quad (2)$$

The full mathematical formulation of the model is presented in Eq. (1). In this equation, S_k represents the measured diffusion-weighted signal for the kth acquisition, and S_0 is the corresponding non-diffusion-weighted signal. Thus, the ratio S_k/S_0 represents the normalized diffusion-weighted signal. b_k denotes the kth diffusion-encoding magnitude (b-value) and $\mathbf{g_k}$ the associated unit gradient direction. $\mathbf{D_i}$ is the ith isotropic tensor characterized by its scalar diffusivity D_i, whereas $\mathbf{D_j}$ is the jth cylindrically symmetric anisotropic tensor with axial diffusivity $\lambda_\parallel$ and radial diffusivity $\lambda_\perp$. M and N are

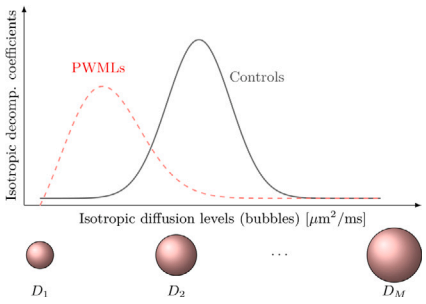

Fig. 2. Conceptual DBM Isotropic Diffusion Spectrum Curves. These illustrative DBM-derived curves compare isotropic diffusion spectrum for tissues affected by punctate white matter lesions (PWMLs, dashed red) and healthy control tissues (Controls, gray). The *x*-axis represents isotropic bubble diameters (diffusion levels), and *y*-axis shows isotropic decomposition coefficients. This paper hypothesized curve shifts happened in the PWMLs compared to controls, because of restricted diffusion in PWMLs.

the numbers of isotropic and anisotropic components, respectively. The anisotropic adjustment term is optional, so N can be set to zero when needed. The coefficients f_{D_i} and f_{D_j} characterize the relative contributions of the ith isotropic and jth anisotropic diffusion components, respectively; by construction, their sums over all components equal to one.

On the right-hand side of the equation, the model separates the signal into two terms: an isotropic term (highlighted in red) and an anisotropic adjustment term (highlighted in blue). The isotropic term represents diffusion that occurs equally in all directions, modeled as a series of isotropic diffusion tensors with varying effective diameters D_i. By spanning a range of diffusion scales, this approach provides a more nuanced characterization of isotropic diffusion, rather than relying solely on standard scalar metrics like AD, RD, or MD.

The anisotropic adjustment term accounts for averaged effects of directional diffusion, as commonly observed in white matter tracts and part of gray matter. The role of the anisotropic term is twofold: (1) to minimize the influence of anisotropic diffusion on the isotropic signal, ensuring a more stable and accurate decomposition of the isotropic diffusion signal; (2) to capture the direction-specific diffusion information associated with anisotropic tissues.

2.2. Algorithm for solving the model's parameters

The DBM algorithm involves determining both isotropic and anisotropic diffusion components. The ultimate goal of the algorithm is to set appropriate values for D_i and D_j (Eq. (1)) and to estimate their corresponding coefficients f_{D_i} and f_{D_j} for further analysis.

2.2.1. Part 1: Anisotropic term adjustment

This step focuses on estimating the anisotropic diffusion tensors $\mathbf{D_j}$ and their coefficients f_{D_j}. We first reformulated the model into Eq. (3), representing the diffusion-weighted signal originating from anisotropic components, and Eq. (5) measuring the average absolute deviation (loss) between the sphericity of each decomposed isotropic tensor and 1.

The underlying premise is that optimal values of f_{D_j} and D_j will accurately capture anisotropic diffusion, thereby minimizing its contribution to the overall signal. This reduction allows the isotropic tensors $\mathbf{D_i}$, derived from Eq. (4), to become more spherical (sphericity approaching 1), thus enhancing the reliability of the isotropic decomposition.

$$S_{aniso} = \sum_{j=1}^{N} f_{D_j} e^{-b_k \mathbf{g_k^T D_j g_k}} \tag{3}$$

$$S_k/S_0 - S_{aniso} = \sum_{i=1}^{M} f_{D_i} e^{-b_k \mathbf{g_k^T D_i g_k}} \tag{4}$$

$$Loss = \frac{1}{M} \sum_{i=1}^{M} |sphericity(\mathbf{D_i}) - 1| \tag{5}$$

To simplify calculations and reduce computational load, we used a single, highly anisotropic, cylindrical-like tensor (White et al., 2013; Ramirez-Manzanares et al., 2007). This tensor effectively extracted anisotropic signal components while exerting minimal influence on the isotropic estimates. Specifically, we set the eigenvalues to $\lambda_1 = 3.10$ μm²/ ms (slightly above typical CSF diffusivity of 3.0 μm²/ ms) along the principal fiber direction, and $\lambda_2 = \lambda_3 = 0.05$ μm²/ ms, for the perpendicular directions, forming a long, thin cylindrical profile (Kingsley, 2006). The principal diffusion directions (eigenvectors) for these anisotropic tensors were derived from standard DTI reconstructions, where $\vec{V}_1$ is the primary eigenvector indicating the principal diffusion direction (Kingsley, 2006).

We then iteratively optimized the anisotropic coefficient f_{D_j} from 0 to 0.99 in increments of 0.005 (Eq. (3)) to estimate the isotropic diffusion tensors $\mathbf{D_i}$ (Eq. (4)), using the loss function defined in Eq. (5) as a guide. For simplicity and computational efficiency, we employed a single anisotropic tensor ($N = 1$) and a single isotropic tensor ($M = 1$) in this step, leading to loss = |1 − sphericity|).

2.2.2. Part 2: Determining isotropic diffusion coefficients

After determining the anisotropic terms (f_{D_j} and D_j), we incorporated them back into Eq. (1), simplifying the model to its isotropic component (Eq. (4)). Since the anisotropic contribution is now known, the isotropic model was effectively linear with respect to the isotropic diffusion values D_i.

Physiological plausibility is ensured by constraining D_i within a range from 0.1 μm²/ ms (below typical intracellular diffusivity) to 3.2 μm²/ ms (above typical CSF diffusivity). We tested various intervals Δd between neighboring D_i values (0.15, 0.20, 0.25, 0.30, and 0.35 μm²/ ms) in different tissue types (gray matter, white matter, and CSF) to identify a small interval that yields both stable isotropic decomposition curves and high diffusion resolution.

With the isotropic diffusion array D_i determined, we computed the coefficients f_{D_i} via a non-negative least-squares fit, and normalized them so their sum equals one. Plotting these coefficients against their corresponding diffusion values D_i produces the isotropic decomposition curve (Fig. 2).

Because no universally accepted diffusivity cut-offs exist for separating restricted and non-restricted diffusion within a voxel, we summarized the isotropic spectrum with a set of shape-based metrics rather than fixed thresholds (Wang et al., 2015; Ye et al., 2020; Lin et al., 2019). Specifically, for every voxel we calculated *Main peak value* ($f_{D_{peak}}$): the coefficient at the curve's highest point, indicating the dominant diffusion fraction within the voxel; *Main peak diffusion Position* (D_{peak}): the diffusion level at which the main peak occurs, revealing the predominant diffusion scale in the tissue; *Full Width at Half Maximum* (FWHM): the width of the curve at half its maximum height, illustrating how uniformly the diffusion is distributed around the main peak; $\frac{1}{4}/\frac{1}{2}/\frac{3}{4}$ *area positions*: the diffusion values at which the cumulative area under the curve reaches 25%, 50%, and 75% of the total, respectively. These thresholds help identify shifts in the distribution of isotropic diffusion compartments; *Fast diffusion coefficients*: the sum of coefficients at higher D_i values, representing the fraction of rapid diffusion components within the voxel. These spectrum-pattern metrics provide a robust, threshold free description of systematic shifts in the isotropic profile. Averaged within lesion, contralateral, and control regions of interest, they allow us to test the hypothesis that PWMLs induce measurable alterations in the isotropic diffusion decomposition curves.

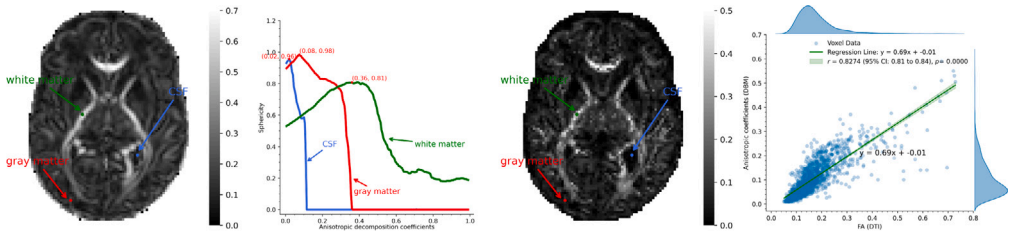

(a) FA (DTI) (b) Anisotropic coeff. fitting (c) Aniso. coeff. map (DBM) (d) Aniso. coefficient and FA

Fig. 3. Locations and anisotropic coefficient fitting for representative voxels. (a) Locations of the three representative voxels on Fractional Anisotropy (FA). (b) Calculation process for isotropic sphericity by looping anisotropic coefficients from 0 to 0.99 in steps of 0.005. (c) Corresponding anisotropic coefficient map. (d) Scatter plot of anisotropic coefficients versus FA values with regression line.

2.3. Subjects

We used MR imaging data from the Developing Human Connectome Project (dHCP) dataset, which was collected at the Center for the Developing Brain, King's College London with the approval of the United Kingdom Health Research Authority (Bastiani et al., 2019; Makropoulos et al., 2018). We included in this study 20 infants with punctate white matter lesions localized to the optic radiation. At the time of scanning, these infants had a mean gestational age (GA) of 37.82±3.00 weeks, and their mean GA at birth was 35.57±3.76 weeks. For comparison purposes, we selected 20 healthy control infants from the same database matching scanning age, GA at birth, birth weight, and sex, to ensure balanced matching against the PWML group. The control group had a mean GA at scan of 37.97±2.84 weeks and a mean GA at birth of 35.79±3.75 weeks. Additionally, for within-subject analyses, the contralateral (no-clear-lesioned) regions of the PWML group were examined as an internal control.

Infants with confirmed PWMLs were identified through a rigorous evaluation process conducted by four trained researchers from our laboratory. Infants with PWMLs were identified based on hallmark imaging patterns of PWMLs, including hyperintensity on T1w images, hypointensity on T2w images, localized to one side of the optic radiation.

All neonates underwent both diffusion MRI and structural MRI scans using a 3T Philips Achieva MRI scanner. The resolution for T2w images was 0.5 mm × 0.5 mm × 0.5 mm with repetition time (TR) of 12,000 ms and echo time (TE) of 156 ms (Makropoulos et al., 2018). Diffusion MRI data included 20 *b*0 images and three diffusion-weighting shells (40 $b = 400$ s/mm^2, 88 $b = 1000$ s/mm^2, and 128 $b = 2600$ s/mm^2), with a spatial resolution of 1.172 mm × 1.172 mm × 1.5 mm. The acquisition was performed with TR / TE of 3800 / 90 ms (Bastiani et al., 2019).

2.4. Data processing

To align structural and diffusion MRI data, T1w and T2w images from each scan were registered with each other and aligned with the diffusion MRI space (Jenkinson et al., 2002; Greve and Fischl, 2009). After ensuring proper alignment, regions of interest (ROIs) were defined on color-coded FA maps as well as on T1w and T2w images. ROIs were drawn to encompass the entire extent of the lesion in order to include multiple voxels per lesion; if the area of the lesion appeared different on the various imaging maps, the lesion boundary defined by T1w served as the standard reference. Corresponding ROIs were then placed in the anatomically equivalent locations on the contralateral side of the same infant's brains and in matched control infant's brains, ensuring a consistent basis for comparison.

Next, the Diffusion Bubble Model was applied to the diffusion MRI data to generate isotropic and anisotropic coefficient maps. Main DBM metrics were calculated for each voxel, including main diffusion positions, FWHM, left and right FWHM diffusion positions, quarter, half, and three-quarter area diffusion positions, and fast diffusion coefficients (see example in Fig. 4). These metrics were then averaged within each ROI for subsequent comparative analysis.

To benchmark DBM against established methods, we fitted the open-source FWE model to the same diffusion data. In both model, the fast (free-water–dominated) compartment was defined as having an isotropic diffusivity $D \geq 2.5$ μm^2/ms, consistent with prior work (Kim et al., 2025; Isaacs et al., 2021; Pasternak et al., 2009). For DBM, the fast-diffusion fraction was obtained by integrating all isotropic-spectrum coefficients f_{D_i} with D_i above this threshold.

Standard diffusion-tensor imaging (DTI) metrics (AD, RD, MD and FA) were extracted using the weighted-least-square DTI reconstruction method (Chung et al., 2006). These DTI metrics serve as the clinical baseline against which the additional sensitivity of DBM (and its comparison with FWE) is evaluated.

2.5. Experiment design and statistics

We conducted two primary experiments to evaluate the performance of the Diffusion Bubble Model.

2.5.1. Parameter optimization and validation using representative tissue types

To determine optimal parameters for DBM, we selected representative voxels from three distinct tissue types: cortical gray matter, white matter, and cerebrospinal fluid, as illustrated in Fig. 3.

First, we focused on the anisotropic component using the algorithm described in Section 2.2 part 1. We hypothesized that CSF, with its high free-water content, would exhibit near-zero anisotropic coefficients, corresponding to isotropic diffusion and very low FA values. Likewise, cortical gray matter, containing relatively more free water and fewer myelinated fibers than white matter, was also expected to have low anisotropic coefficients. In contrast, white matter, characterized by organized, myelinated fiber tracts and lower free-water content, should display higher anisotropic coefficients. By plotting these coefficients against FA values and performing regression analyses, we aimed to confirm that the anisotropic coefficients derived from DBM accurately capture tissue-specific anisotropy.

Next, we optimized the isotropic diffusion parameters by varying the diffusion interval step size Δd among 0.15, 0.20, 0.25, 0.30, and 0.35 μm^2/ ms with a diffusion range of 0.1 to 3.2 μm^2/ ms. By examining how different interval steps influenced the isotropic decomposition curves for each tissue type, we identified the smallest interval that provided the most stable and discriminative results.

Finally, we applied DBM parameters to the representative voxels of each tissue type and extracted the resulting DBM-derived metrics. We then compared these metrics against DTI metrics, using this limited set of representative voxels to evaluate DBM's ability to distinguish microstructural differences more effectively than DTI. Although this analysis is not exhaustive, it provides an initial indication that DBM may offer a more nuanced and accurate characterization of underlying tissue properties compared to standard DTI metrics.

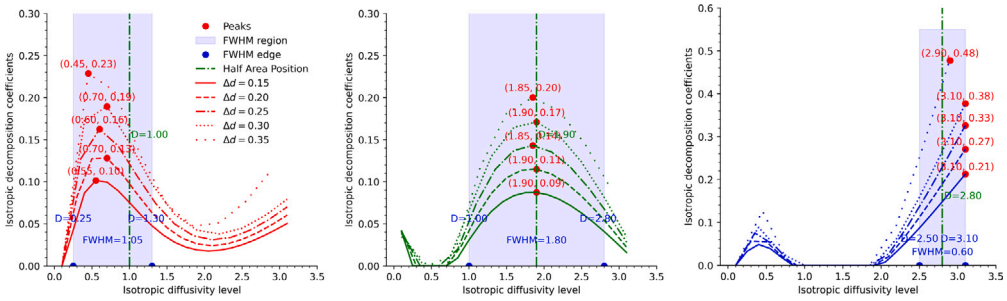

(a) Gray matter (b) White matter (c) CSF

Fig. 4. Fitting results for individual voxels in: (a) Cortical gray matter; (b) White matter; (c) Cerebrospinal fluid (CSF). For each voxel, the isotropic decomposition coefficient curves are displayed using different isotropic diffusion interval steps Δd of 0.15, 0.20, 0.25, 0.30, and 0.35 $\mu m^2/$ ms within a diffusion range of 0 to 3.2 $\mu m^2/$ ms. These curves illustrate how varying Δd affects the stability and distinguishability of the isotropic decomposition for each tissue type.

2.5.2. Detecting and characterizing PWMLs

After validating DBM's effectiveness, we utilized DBM metrics and curves to explore potential subgroups within punctate white matter lesions.

To investigate whether DBM could detect microstructural differences associated with these PWML subtypes, we conducted comparisons of DBM-derived diffusion coefficient curves between ROIs in PWML group and healthy control group using paired t-tests ($p < 0.05$) within each subgroup. Additionally, we performed within-subject comparisons by examining corresponding contralateral ROIs in the contralateral group, again utilizing paired t-tests ($p < 0.05$).

We hypothesized that PWMLs would induce a leftward shift in the isotropic diffusion decomposition coefficient curves, reflecting restricted diffusion and underlying microstructural damage (Fig. 2). By comparing lesion sites to both contralateral regions and healthy controls, we aimed to confirm that DBM metrics effectively capture subtle tissue changes specifically linked to PWMLs.

For a comprehensive assessment, we also analyzed conventional DTI metrics to detect differences among lesion, contralateral, and control groups within each PWML subtype. By comparing DBM and DTI findings, we assessed DBM's added value in identifying and characterizing PWML-related tissue alterations.

3. Results

3.1. Parameter optimization and validation using representative tissue types

Through iterative optimization of the anisotropic coefficient from 0 to 0.99 in 0.005 increments, we identified distinct result values for each tissue type (Fig. 3(b)). Sphericity peaked at 0.98 for gray matter, 0.81 for white matter, and 0.96 for CSF, corresponding to optimal anisotropic coefficients of 0.09, 0.36, and 0.02, respectively. These values align with known tissue properties: minimal anisotropy in CSF, low anisotropy in gray matter, and higher anisotropy in white matter. DBM-derived anisotropic coefficients exhibited a strong correlation with FA values ($r = 0.8274$, $p < 0.0001$) (Fig. 3(d)) and anisotropic coefficient map closely resembled the FA map (Fig. 3(c)), confirming that DBM effectively captures anisotropic diffusion properties.

Isotropic decomposition curves were generated using diffusion interval steps (Δd) of 0.15, 0.20, 0.25, 0.30, and 0.35 $\mu m^2/$ ms (Fig. 4). Although changes in Δd affected coefficient magnitudes, the overall curve shapes and peak positions of the isotropic decomposition curves remained consistent across tissue types, preserving their discriminative features. We selected the smallest $\Delta d = 0.15$ $\mu m^2/$ ms for subsequent analyses.

3.2. Comparison of DBM and DTI metrics across tissue types

DTI and DBM metrics were compared in representative white matter, gray matter, and CSF voxels (Table 1). DBM metrics showed greater percentage differences between tissue types than DTI metrics. For example, the anisotropic coefficient difference between white matter and gray matter reached 86.1%, compared to a 76.5% difference in FA. Similarly, the main diffusion position (DBM metric) exhibited a 52.2% difference between white and gray matter, surpassing differences observed with AD (36.9%), RD (42.4%), and MD (4.1%). The left boundary of FWHM of isotropic diffusion decomposition coefficient curve showed a 525.0% difference between white matter and CSF, far exceeding differences observed with DTI metrics. These findings indicate that DBM provides enhanced sensitivity in characterizing tissue microstructure.

3.3. Fast water diffusion components

3.3.1. Evaluation of fast water diffusion elimination performance

We compared DBM derived fast water diffusion coefficients with those obtained from the Free Water Elimination model (Fig. 5). Across all tissue types, DBM coefficients correlated strongly with FWE results (e.g., all voxels combined: $r = 0.9319$, $p < 0.0001$; Gray matter: $r = 0.8447$, $p < 0.0001$). Similar strong correlations were observed for white matter, and CSF. These high correlations and narrow confidence intervals confirm that DBM effectively separates fast water diffusion components, in close agreement with established FWE methods.

3.3.2. Identification of PWML subtypes based on fast diffusion coefficients

Applying DBM to punctate white matter lesions in optic radiation revealed two distinct lesion subtypes, differentiated by their fast diffusion coefficients:

Wet-Type PWMLs (wet lesions): These lesions exhibited elevated fast diffusion coefficients relative to both contralateral and control regions, suggesting higher free water content.

Dry-Type PWMLs (dry lesions): These lesions did not show elevated fast diffusion coefficients compared to contralateral and control tissues, potentially reflecting different pathologies such as chronic gliosis without substantial free water accumulation.

Fig. 6 illustrated these findings. Wet lesions (pink circles) consistently showed higher fast diffusion coefficients across scanning ages, whereas dry lesions (red circles) more closely resembled contralateral (orange triangles) and control (gray squares) regions. All groups demonstrated a decreasing trend in fast diffusion coefficients with increasing scanning age, consistent with normal neonatal brain maturation and a gradual reduction in free water content (Jelescu et al., 2020).

Of the 20 PWML cases analyzed, 10 were classified as wet lesions and 10 as dry lesions. Although their gestational ages at scanning were

Table 1
Comparison of DTI and DBM Metrics for Representative Voxels of White Matter, Gray Matter, and Cerebrospinal Fluid. This table presents the absolute values of Diffusion Tensor Imaging (DTI) and Diffusion Bubble Model (DBM) metrics for representative voxels of three different tissue types: white matter, cortical gray matter, and cerebrospinal fluid (CSF). For each metric, the absolute value is displayed. Additionally, the absolute and percentage differences between gray matter and white matter, as well as between CSF and white matter, are calculated to highlight the contrast in diffusion properties among the tissues.

	White matter	Gray matter			CSF		
	WM	GM	GM−WM	$\frac{100(GM-WM)}{WM}$	CSF	CSF−WM	$\frac{100(CSF-WM)}{WM}$
	$\mu m^2/ms$	$\mu m^2/ms$	$\mu m^2/ms$	%	$\mu m^2/ms$	$\mu m^2/ms$	%
AD (DTI)	1.85	1.17	−0.68	−36.89	2.59	0.74	40.17
RD (DTI)	0.65	0.93	0.28	42.38	2.26	1.60	245.08
MD (DTI)	1.05	1.01	−0.04	−4.07	2.37	1.32	125.02
FA (DTI)	0.58	0.14	−0.45	−76.50	0.09	−0.49	−84.03
Aniso. coefficient	0.36	0.05	−0.31	−86.11	0.02	−0.34	−94.44
Main diff. position	1.15	0.55	−0.60	−52.17	3.10	1.95	169.57
Peak value	0.07	0.10	0.04	55.80	0.21	0.15	226.60
FWHM	1.80	1.05	−0.75	−41.67	0.60	−1.20	−66.67
Left FWHM	0.40	0.25	−0.15	−37.50	2.50	2.10	525.00
Right FWHM	2.20	1.30	−0.90	−40.91	3.10	0.90	40.91
1/4 area position	1.00	0.70	−0.30	−30.00	2.50	1.50	150.00
1/2 area position	1.30	1.00	−0.30	−23.08	2.80	1.50	115.38
3/4 area position	1.75	2.05	0.30	17.14	2.95	1.20	68.57

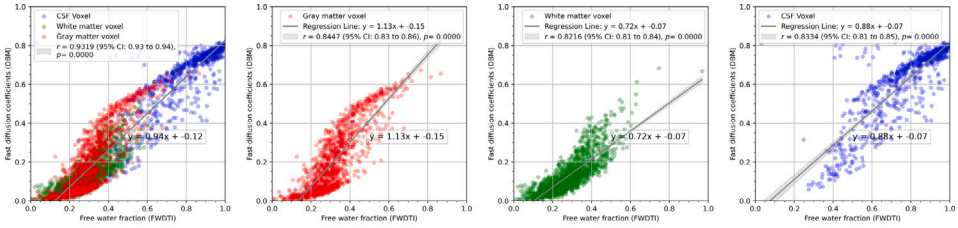

(a) All voxel (b) Gray matter (c) White matter (d) CSF

Fig. 5. Evaluation of Fast Water Diffusion Elimination Performance Compared to the Free Water Elimination (FWE) Model . This figure presents scatter plots comparing the fast water diffusion coefficients derived from our model with the free water fraction (FWDTI) obtained from the FWE model: (a) Scatter plot for all voxels; (b) Scatter plot in gray matter; (c) Scatter plot in white matter; (d) Scatter plot in cerebrospinal fluid (CSF).

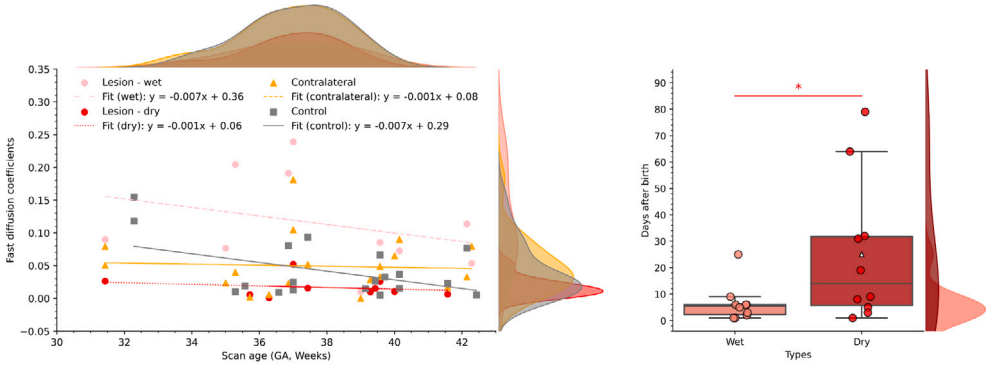

(a) Fast Diffusion Coefficient vs. Scan Age (b) Days after birth of subtypes

Fig. 6. Age-Related patterns of Fast Diffusion Coefficients and days after birth at MRI in PWML Subtypes. (a) Scatter plot of the fast diffusion coefficient versus scanning age for different groups: wet-type PWMLs (pink circles), dry-type PWMLs (red circles), contralateral regions (orange triangles), and control regions (gray squares). Trend lines are fitted for each group to illustrate how fast diffusion coefficients vary across scanning ages. (b) Box plot of days after birth for wet-type (pink) and dry-type (red) PWMLs (Mann–Whitney, one-sided, wet < dry: $U = 26.0$, $p = 0.0376$). The center line indicates the median; open triangle indicates mean; box limits represent the upper and lower quartiles; whiskers extend to 1.5× the inter-quartile range.

similarly distributed (Fig. 6(a) top), a box plot of days after birth (Fig. 6(b)) revealed significantly shorter postnatal ages at MRI for wet-type (pink) compared to dry-type (red) PWMLs (median of 5.50 days for wet type *vs.* 14.00 days for dry, Mann–Whitney, wet < dry: $U = 26.0$, $p = 0.0376$). Subsequently, these subtypes were used for further analysis, enabling a more nuanced understanding of the pathology and development of PWMLs.

3.3.3. *Examples of wet- and dry-type PWMLs*

To illustrate the distinct diffusion profiles of wet- and dry-type PWMLs, we present two representative cases, each displaying T1w, T2w, and MD images, along with DBM decomposition maps at selected diffusion levels, and all on the same axial slice containing the PWML in the optic radiation.

A wet-lesion example in the optic radiation is shown in Fig. 7 from a newborn scanned at 35.00 weeks GA (born at 34.14 weeks). Consistent with previous reports (Nguyen et al., 2019; Niwa et al., 2011; Hayman et al., 2019), the lesion appeared hyperintense on T1w, hypointense on T2w, and restricted diffusion on MD maps. At various DBM diffusion levels: (a) $D = 0.25$ $\mu m^2/$ ms: Lesion was clearly brighter than the contralateral side. (b) $D = 1.00$ $\mu m^2/$ ms: Signal intensifies further. (c) $D = 2.35$ $\mu m^2/$ ms: A distinctly darker region emerged. (d) $D = 3.10$ $\mu m^2/$ ms: Elevated fast diffusion components appeared.

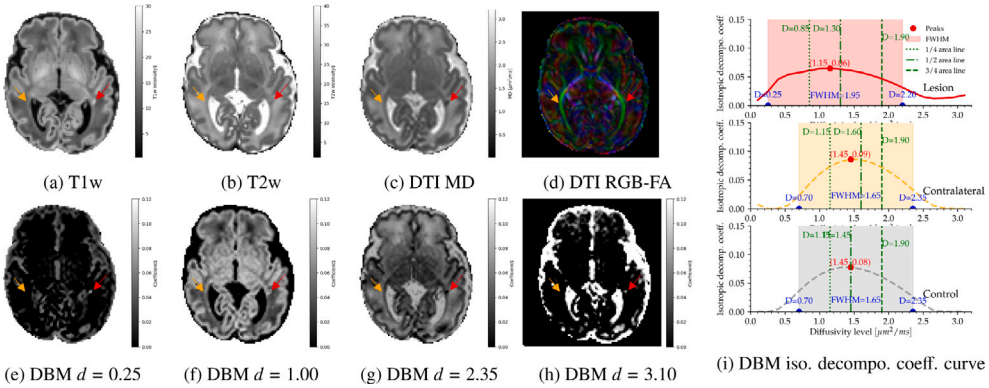

Fig. 7. Visualization of a Wet-Type PWMLs in the optic radiation using DTI and DBM. (a)–(d) Lesion appearance on: T1-weighted (T1w), T2-weighted (T2w), Mean Diffusivity (MD), and RGB-FA images. (e)–(h) Diffusion Bubble Model decomposition maps at diffusion levels: D = 0.25, 1.15, 2.35, and 3.10 $\mu m^2/$ ms. Red arrows indicate the PWML lesion, while orange arrows point to the contralateral (non-lesion) region. The control region of interest (ROI), not shown here, is located in a matched control subject. (i) Isotropic decomposition coefficient curves for the lesion, contralateral, and control ROIs, illustrating differences in diffusion properties among the regions. The infant was born at gestational age of 34.14 weeks and scanned at 35.00 weeks gestational age.

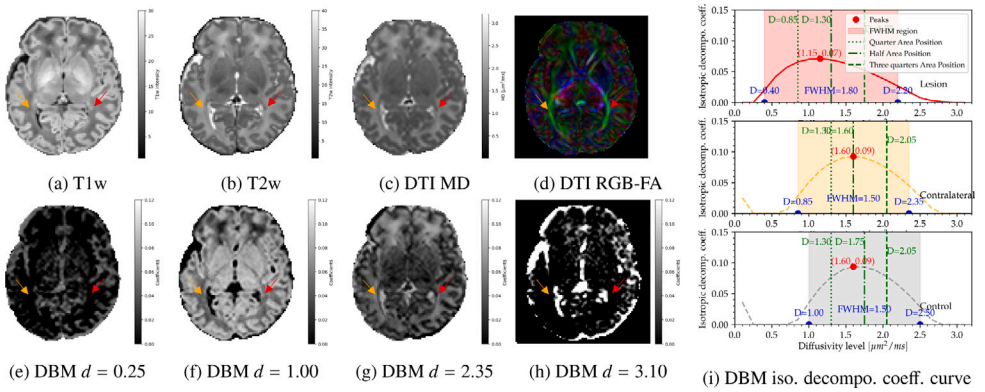

Fig. 8. Visualization of a Dry-Type PWMLs in the Optic Radiation Using DTI and DBM. (a)–(d) Lesion appearance on: T1-weighted (T1w), T2-weighted (T2w), Mean Diffusivity (MD), and RGB-FA images. (e)–(h) Diffusion Bubble Model (DBM) decomposition maps at diffusion levels: D = 0.25, 1.15, 2.35, and 3.10 $\mu m^2/$ ms. Red arrows indicate the PWML lesion, while orange arrows point to the contralateral (non-lesion) region. The control region of interest (ROI), not shown here, is located in a matched control subject. (i) Isotropic decomposition coefficient curves for the lesion, contralateral, and control ROIs, illustrating differences in diffusion properties among the regions. The infant was born at gestational age of 39.29 weeks and scanned at 39.43 weeks gestational age.

The isotropic decomposition coefficient curves (Fig. 7(i)) highlighted key differences between lesion and non-lesion regions. In particular, the lesion's 1/4 and 1/2 area lines shift leftward, and its FWHM expanded compared to contralateral and control regions. These changes imply an altered microstructure and increased free water content, aligning with an edema-like or acute inflammatory state.

A dry-lesion example in the optic radiation is shown in Fig. 8 from a newborn scanned at 39.43 weeks GA (born at 39.29 weeks). The lesion also appeared hyperintense on T1w, hypointense on T2w, and restricted on MD, but at the highest and lowest diffusion levels (D = 0.25 $\mu m^2/$ ms and D = 3.10 $\mu m^2/$ ms), the lesion did not visibly differ from contralateral tissue, unlike the wet-lesion example. Differences were observed at intermediate diffusion levels (D = 1.00 $\mu m^2/$ ms and D = 2.35 $\mu m^2/$ ms), indicating microstructural alterations with less free water accumulation.

The corresponding isotropic decomposition curves (Fig. 8(i)) confirmed these observations: while the lesion demonstrated a leftward shift in the 1/4 and 1/2 area lines and a wider FWHM relative to contralateral and control regions (similar to the wet lesion), there was no significant elevation of fast diffusion components. This profile suggests a different pathological mechanism, likely involving structural changes without prominent edema.

3.4. Group-level analysis of Lesion, Contralateral, and Control Regions using DBM

Averaged isotropic decomposition coefficient curves from 20 infants with PWMLs in the optic radiation (10 wet PWMLs and 10 dry PWMLs) were shown in Fig. 9. Quantitative DBM metrics, including main diffusion position, anisotropic coefficient, FWHM, were summarized in Fig. 10, while corresponding DTI results were presented in Fig. 11.

3.4.1. DBM spectrum curve analysis

The averaged DBM curves (Fig. 9) revealed notable differences among lesion, contralateral, and control regions:

Combined group. Compared to contralateral and control regions, lesion regions showed a leftward shift in both the 1/4 and 1/2 area lines. Specifically, the 1/4 area line shifted from 1.30 $\mu m^2/$ ms in controls to 1.15 $\mu m^2/$ ms (contralateral) and 0.85 $\mu m^2/$ ms (lesion), while the 1/2 area line shifted from 1.60 $\mu m^2/$ ms (control and contralateral) to 1.30 $\mu m^2/$ ms (lesion). This pattern suggested an increased proportion of slower diffusion components.

Wet PWMLs. These lesions showed more pronounced leftward shifts at the slower diffusion thresholds (e.g., 1/4 area line) and substantial increases in fast diffusion coefficients, consistent with elevated free water content in the individual wet-type PWML example.

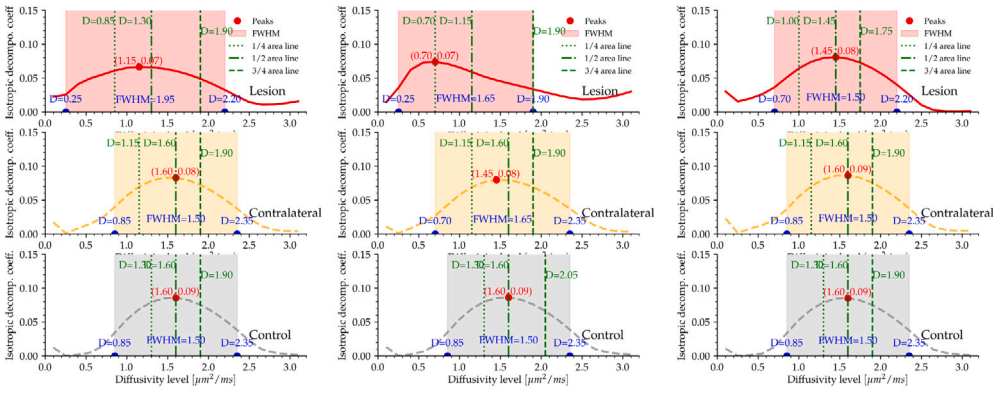

(a) Combined-Type PWMLs (b) Wet-Type PWMLs (c) Dry-Type PWMLs

Fig. 9. Averaged Isotropic Decomposition Coefficient Curves for Lesion, Contralateral, and Control Regions in the Optic Radiation. This figure presents the averaged isotropic decomposition coefficient curves within the optic radiation for: (a) Subjects with both Type 1 (wet) and Type 2 (dry) punctate white matter lesions (PWMLs) ($N = 20$); (b) Subjects with only Wet-type PWMLs ($N = 10$); (c) Subjects with only Dry-type PWMLs ($N = 10$). Lesion Regions: Red solid curve; Contralateral Regions: Orange dashed curve, from the same subjects as the lesion regions; Control Regions: Gray dashed curve, from 20 paired healthy controls.

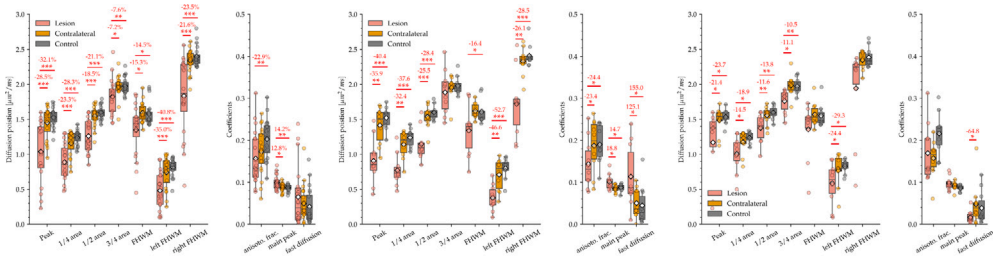

(a) Combined-Type PWMLs (b) Wet-Type PWMLs (c) Dry-Type PWMLs

Fig. 10. Bar Graphs of Key DBM Metrics in the Optic Radiation Comparing Lesion, Contralateral, and Control Regions. This figure illustrates key Diffusion Bubble Model (DBM) metrics in the optic radiation, comparing lesion regions (red bars), contralateral regions (orange bars), and control regions from matched healthy subjects (gray bars). (a) All subjects with punctate white matter lesions (PWMLs) ($N = 20$), (b) Subjects with only Type 1 (wet) PWMLs ($N = 10$), and (c) Subjects with only Type 2 (dry) PWMLs ($N = 10$). Statistically significant differences are indicated by * ($p < 0.05$), ** ($p < 0.01$), and *** ($p < 0.001$), with the magnitude of changes shown above the significance markers.

Dry PWMLs. While also shifting toward slower diffusion domains, dry-type PWMLs exhibited less pronounced shifts at the 1/4 area line, and did not display significant increases in fast diffusion components, mirroring the pattern seen in individual dry-type PWML example case.

3.4.2. Differences in DBM metrics

Key DBM metrics (Fig. 10) further illustrate the distinction between wet and dry PWMLs. Compared to control and contralateral regions, lesion regions consistently exhibit shifts toward slower diffusion domains; wet lesions additionally show elevated fast diffusion components, whereas dry lesions display more moderate alterations without a pronounced increase in fast diffusion.

1/4 *area line.* Combined group lesions showed a 28.3% reduction relative to controls and a 23.3% reduction relative to contralateral regions. Wet lesions showed even larger reductions of 37.6% (*vs.* controls) and 32.4% (*vs.* contralateral). Dry lesions show moderate reductions of 18.9% (*vs.* controls) and 14.5% (*vs.* contralateral).

1/2 *area line.* The combined group exhibited a 21.1% reduction compared to controls and an 18.5% reduction compared to contralateral. Wet lesions displayed more pronounced reductions of 28.4% (*vs.* controls) and 25.5% (*vs.* contralateral). Dry lesions showed a smaller reduction of 13.8% (*vs.* controls) and 11.6% (*vs.* contralateral).

Fast diffusion coefficients. Wet Lesions showed a marked increase in fast diffusion coefficients, reaching 155.0% above control levels and 125.1% above contralateral levels, indicating edema-like changes. Dry Lesions, contrarily, exhibited a 64.8% decrease compared to contralateral regions and no significant difference compared to controls.

Anisotropic decomposition coefficients. The combined group showed a 22.9% reduction relative to controls and no significant change compared to contralateral. Wet lesions exhibited reductions of 24.4% versus controls and a 23.4% versus contralateral, suggesting diminished anisotropy. Dry lesions showed no significant reductions compared to either control or contralateral tissue.

3.4.3. Comparison of DTI metrics

When examining DTI metrics in the combined PWML group (Fig. 11(a)), lesion regions showed moderate reductions compared to controls and contralateral regions. Specifically, AD decreased by 28.5% compared to controls and 25.5% compared to contralateral regions. RD and MD followed similar decreases of roughly 25–27%.

Wet-Type PWMLs For wet-type lesions (Fig. 11(b)), AD was reduced by 31.9% and 31.6% compared to control and contralateral regions, respectively, suggesting changes in axonal integrity or intracellular water content. RD decreased by 29.0% (*vs.* controls) and 26.9% (vs. contralateral), while MD declined by 30.3% (*vs.* controls) and 29.0% (*vs.* contralateral). FA also dropped by 14.5% and 16.9% compared to controls and contralateral regions, respectively.

Dry-Type PWMLs By contrast, dry-type lesions (Fig. 11(c)), exhibited somewhat smaller overall reductions in AD, RD, and MD than wet-type lesions. AD was reduced by 25.2% compared to the control group and 19.1% compared to the contralateral group. RD decreased by 21.6% (*vs.* controls) and 23.4% (*vs.* contralateral), and MD was reduced by 23.2% (*vs.* controls) and 21.5% (*vs.* contralateral). These figures indicate moderate but less extensive disruption of diffusion properties compared to wet lesions.

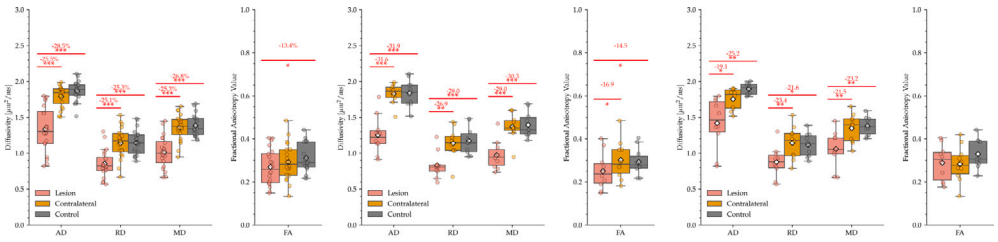

(a) Combined-Type PWMLs (b) Wet-Type PWMLs (c) Dry-Type PWMLs

Fig. 11. DTI Bar Graph Comparing AD, RD, MD, and FA in the Optic Radiation Comparing Lesion (red), Contralateral (orange), and Control Regions (gray). (a) All subjects with punctate white matter lesions (PWMLs) ($N = 20$), (b) Subjects with only Type 1 (wet) PWMLs ($N = 10$), and (c) Subjects with only Type 2 (dry) PWMLs ($N = 10$). Statistically significant differences are marked as * ($p < 0.05$), ** ($p < 0.01$), and *** ($p < 0.001$), with the value differences displayed above the corresponding significance markers.

4. Discussion

In this study, we introduced the Diffusion Bubble Model, a novel diffusion MRI model designed to provide more nuanced detection and assessment of tissue microstructural alterations than regular MRI methods. Our approach decomposes the diffusion-weighted signal into isotropic and anisotropic components, generating a continuous distribution of isotropic "bubbles" and capturing anisotropic information without constraining the number or geometry of anisotropic components. This decomposition allows DBM to characterize broader diffusion behaviors within tissues, providing complementary insights beyond those afforded by DTI.

4.1. Diffusion Bubble Model performance

Applying DBM to three representative tissue types (gray matter, white matter, and CSF) demonstrated its enhanced capability to distinguish microstructural differences compared to conventional DTI metrics. Although some variability was noted in the anisotropic decomposition coefficient (fraction) maps (Fig. 3(b)), DBM-derived anisotropic coefficients strongly correlated with FA values in representative tissue voxels (Pearson's $r = 0.8274, p < 0.0001$; Fig. 3(d)). The anisotropic decomposition revealed a clear global peak, with tissues exhibiting expected anisotropy patterns: CSF approached zero anisotropic fraction; gray matter showed moderate anisotropy; and myelinated white matter displayed higher anisotropic fractions. Although we simplified the anisotropic fitting by using a single cylindrical tensor rather than full ellipsoids, the resulting sphericity in white matter still reached 0.81. This suggests that our simplified approach managed to successfully capture anisotropic information before measuring isotropic parts.

The isotropic decomposition was very robust. Even when varying the interval step size significantly (from 0.15 to 0.35 $\mu m^2/$ ms, Fig. 4), the overall shapes of the isotropic decomposition curves remained consistent, peaking near specific diffusion values for each tissue type (gray matter: 0.55 $\mu m^2/$ ms, white matter: 1.90 $\mu m^2/$ ms, CSF: 3.10 $\mu m^2/$ ms). Additionally, the diffusion position lines shifted left for slower diffusion components, with the exception of the 3/4 area position line, which moved to the right when comparing gray matter to white matter. These findings suggest that gray matter contains more cellular structures (smaller diffusion environments) and possibly higher free water components compared to white matter, aligning with previous literature (Andersson et al., 2020; Motta et al., 2019; Kelly et al., 2022). While DTI metrics (e.g., lower AD, higher RD, and lower FA in gray matter) similarly highlight differences between these tissues, DBM provided a more nuanced picture, capturing increased free water content that is less apparent in DTI.

This enhanced sensitivity was even more evident in analyzing PWMLs. For instance, wet-type PWMLs showed less than 31.9% reduction in DTI compared to the other regions (Fig. 11(b)). In contrast, DBM revealed significantly larger shifts to lower diffusion direction with multiple metrics (−37.6% in 1/4 area line, −52.7% in left FHWM) from the control and contralateral groups to the lesion group (Fig. 10(b)). Moreover, DBM identified substantial increases in fast diffusion (155.0% and 125.1% for wet-type PWMLs relative to control and contralateral groups, respectively) highlighting its ability to detect subtle alterations in tissue composition.

Finally, DBM's capability to assess and eliminate fast diffusion compartments is crucial, given that voxel-level resolution and the underlying microstructure differ by orders of magnitude. By comparing DBM-derived fast diffusion coefficients with those from the Free Water Elimination model, we observed a strong correlation (Fig. 5), confirming that DBM effectively captures and accounts for free water components. These results suggest that DBM provides a more comprehensive and sensitive depiction of tissue microstructure than DTI, offering enhanced diagnostic and research utility.

4.2. Positioning DBM within the dMRI landscape

The Diffusion Bubble Model shares the same core assumption as other multicompartment models, a voxel's diffusion-weighted signal is a sum of multiple monoexponential decays (Wang et al., 2011; Zhang et al., 2012; Palombo et al., 2020; Rodríguez-Soto et al., 2022; Conlin et al., 2021), yet it departs from current frameworks in several decisive ways.

First, relative to Diffusion Basis Spectrum Imaging, DBM collapses orientation coherent signals into a small, optional set of anisotropic tensors and then captures the remaining complexity or remaining signal in a continuous one dimensional isotropic spectrum. DBSI, in contrast, fits a separate anisotropic compartment for every putative fiber population and models the isotropic component as a series of apparent diffusivity terms (Wang et al., 2011; Han et al., 2023). Although this strategy can produce compartment-specific parameters, it substantially increases the number of fit variables and therefore potentially reduces robustness (Han et al., 2023). DBM's spectrum-focused formulation achieves comparable diagnostic sensitivity with fewer parameters, enabling stable reconstructions from three-shell data by using isotropic tensors in fitting. Furthermore, DBM employs an isotropic diffusion spectrum to characterize tissue properties, which is inspired in part by the approach used in DBSI. DBSI has demonstrated that the presence of certain pathological features (e.g., inflammation) can produce a leftward shift in the diffusion spectrum (Wang et al., 2011). DBM extends this concept by using multiple characteristic lines rather than truncating the spectrum at predefined diffusion boundaries, allowing it to capture more nuanced shifts.

Second, when the anisotropic term is suppressed ($M = 0$), DBM superficially resembles RSI; yet DBM differs in two key respects. RSI averages the signal across shells and constrains each isotropic compartment to a fixed apparent diffusivity derived from two- or three-compartment models or empirically (Rodríguez-Soto et al., 2022; Conlin et al., 2021). Although the author claimed that RSI did not explicitly prescribe a particular number of compartments in RSI, the number of compartments was limited (≤ 5, because of the number of b values

during acquisition) for current practical experiments (Rodríguez-Soto et al., 2022; Conlin et al., 2021). DBM, on the contrary, uses a continuous isotropic tensor array, freeing model from assumptions about how many compartments exist or what their diffusivity should be. This flexibility allows DBM to adapt seamlessly to different tissue types without re-tuning isotropic component diffusivity and to preserve directional cues that shell-averaging would otherwise erase.

Third, DBM sits between extremes represented by DSI and strongly biophysical, geometry-specific models such as NODDI or SANDI. DSI reconstructs the entire three-dimensional displacement probability density function using the Fourier transform, but requires hundreds of gradient directions, which is an impractical burden for newborn scanning (Van Jay Wedeen Reese et al., 2000). At the other end of the spectrum, models like NODDI and SANDI hard-code two or three geometric compartments (for example, intra-axonal space, extracellular space, and spherical soma) and thus cannot capture a continuum diffusion spectrum (Zhang et al., 2012; Palombo et al., 2020). DBM bridges this methodological gap by producing a spectrum that reflects continuous variation in different diffusion level without prescribing compartment geometries or imposing prohibitive acquisition requirements.

Although we have not yet optimized DBM for a dedicated acquisition protocol, the three-shell scheme used in the present study already produced stable spectra. In theory, adding more b-values with modest angular coverage sharpens the isotropic spectrum, whereas concentrating directions within fewer shells accentuates the averaged anisotropic term by broadening or shouldering the spectrum. Because DBM's mathematical structure parallels DBSI, existing DBSI protocols, such as 25-direction-and-point acquisitions ($b \leq 1000$–1500 s/mm^2), should translate directly to DBM with scan times of only a few minutes (Zhang et al., 2025; Kim et al., 2025). But a systematic comparison of these acquisition scheme and one-, two-, three-shell schemes for DBM remains an important avenue for future work.

4.3. Two types of PWMLs: Wet-type and dry-type

By decomposing the diffusion signal, DBM revealed that punctate white matter lesions are associated with restricted diffusion, consistent with findings from both DTI and previous studies (Hayman et al., 2019; Nguyen et al., 2019). More importantly, DBM demonstrated for the first time that not all PWMLs share the same microstructural diffusion signatures, even though they present similarly with T1w hyperintensity and T2w hypointensity. Specifically, we identified two distinct lesion subtypes (wet-type and dry-type) on isotropic decomposition curves and fast diffusion components.

Histopathological research on focal white matter injuries has described microhemorrhages, microcalcifications, necrotic areas, and glial cell reactions (Nanba et al., 2007). Early PWMLs often exhibit restricted diffusion attributed to hypercellularity, especially infiltration by activated microglia (Niwa et al., 2011; Rutherford et al., 2010). Our DBM results support this notion while adding further detail:

Wet-Type PWMLs show a pronounced leftward shift in the isotropic diffusion spectrum at slower diffusion levels (the 1/4 area line) and a substantial increase in fast diffusion coefficients. Slower diffusion levels likely reflect intracellular or restricted water compartments (Wang et al., 2011; Brunsing et al., 2017; White et al., 2013), and their shifts suggest edema-like changes and possibly acute inflammation (e.g., glial activation) (Nanba et al., 2007; Zhang et al., 2023). The elevated fast diffusion components may reflect a transient phase of free-water accumulation, as typically seen in edema. This fast water accumulation could also change water molecules compartmentalization, which appears to affect T1w signal more than T2w in neonatal brains (Dubois et al., 2021), explaining why wet-type lesions show greater T1w differences than dry-type, whereas T2w changes are similar across both subtypes (Figs. 7 and 8).

Dry-Type PWMLs, in contrast, display a more uniform leftward shift throughout the diffusion spectrum without a significant elevation in fast diffusion coefficients. This pattern suggests elevated cellularity or chronic structural rearrangements, but with less fast water components. Dry-type lesions may represent a slightly later acute stage where edema subsides, yet cellular changes persist. Consequently, infants with dry-type PWMLs exhibit a longer interval after birth than those with wet-type PWMLs (Fig. 6(b)).

4.4. Clinical implications and future directions

Our findings highlight the Diffusion Bubble Model's ability to detect and differentiate subtypes of punctate white matter lesions, providing valuable additional information for lesion characterization. Despite these promising results, several limitations must be addressed to enhance DBM's utility: (1) Refining anisotropic modeling: further optimizing the anisotropic component of DBM and examining its influence on the isotropic diffusion spectrum can improve the model's sensitivity and specificity; (2) Optimizing MRI acquisition protocols: establishing standardized protocols will help ensure consistent and reproducible data across different clinical settings, thereby strengthening the reliability of DBM-derived metrics; (3) Incorporating histopathological evidence would further reinforce DBM's lesion classification accuracy, especially for preclinical studies; (4) Longitudinal evaluations: applying DBM to repeated scans can offer insights into lesion evolution over time, demonstrating the model's ability to detect dynamic changes of brain injuries and will be of immense help to quantify novel neuroprotection strategies; (5) Future studies that include healthy adults and other age or species cohorts are warranted to confirm both the general performance of DBM and the injury-specific findings reported here. (6) Due to limited available resources, we were unable to quantify intra-subject repeatability for DBM; future studies will therefore include prospective test–retest scans to formally establish reproducibility.

5. Conclusion

This study introduced the Diffusion Bubble Model, a novel MRI approach for detection and subtyping white matter lesions. Using punctate white matter lesions in neonates as a test case, we showed that DBM effectively decomposes diffusion-weighted signals into an averaged anisotropic contribution and a continuum of isotropic diffusion components, then analyze these as an isotropic diffusion spectrum. This approach successfully captured the subtle shifts toward slower diffusion observed in PWMLs within the neonatal optic radiation. Crucially, DBM demonstrated enhanced sensitivity compared to conventional techniques, enabling the distinction between two PWML subtypes (wet-type and dry-type) and offering a more nuanced understanding of lesion pathology.

CRediT authorship contribution statement

Erjun Zhang: Writing – review & editing, Writing – original draft, Visualization, Validation, Methodology. **Benjamin De Leener:** Writing – review & editing, Supervision, Conceptualization. **Gregory A. Lodygensky:** Writing – review & editing, Supervision, Conceptualization.

Declaration of competing interest

The authors declare that they have no known competing financial interests or personal relationships that could have appeared to influence the work reported in this paper.

Acknowledgments

The authors would like to express their sincere gratitude to our lab members, Kylie Xu, Hanna Ton That, and Josephine Emadoye, for their invaluable contributions to the identification of PWMLs. We are also grateful for the financial support provided by the China Scholarship Council. This study was supported by Polytechnique Montreal, by the Canada First Research Excellence Fund, by CHU Sainte-Justine Research Center, by the Quebec BioImaging Network (QBIN) and by the TransMedTech Institute. Data was shared by the developing Human Connectome Project.

Data availability

The data used in this study was obtained from the Developing Human Connectome Project (dHCP), an open-source dataset available to researchers upon approval through the dHCP portal (link). Access to the dHCP data requires registration and compliance with the consortium's data usage agreements.

References

Alexander, A.L., Lee, J.E., Lazar, M., Field, A.S., 2007. Diffusion tensor imaging of the brain. Neurotherapeutics 4 (3), 316–329.

Andersson, M., Kjer, H.M., Rafael-Patino, J., Pacureanu, A., Pakkenberg, B., Thiran, J.-P., Ptito, M., Bech, M., Bjorholm Dahl, A., Andersen Dahl, V., Dyrby, T.B., 2020. Axon morphology is modulated by the local environment and impacts the noninvasive investigation of its structure-function relationship. Proc. Natl. Acad. Sci. USA 117 (52), 33649–33659.

Arberet, C., Proisy, M., Fausser, J.L., Curt, M., Bétrémieux, P., Tréguier, C., Rozel, C., Pladys, P., 2017. Isolated neonatal MRI punctate white matter lesions in very preterm neonates and quality of life at school age. J. Neonatal Perinat. Med. 10 (3), 257–266.

Bastiani, M., Andersson, J.L.R., Cordero-Grande, L., Murgasova, M., Hutter, J., Price, A.N., Makropoulos, A., Fitzgibbon, S.P., Hughes, E., Rueckert, D., Victor, S., Rutherford, M., Edwards, A.D., Smith, S.M., Tournier, J.-D., Hajnal, J.V., Jbabdi, S., Sotiropoulos, S.N., 2019. Automated processing pipeline for neonatal diffusion MRI in the developing human connectome project. Neuroimage 185, 750–763.

Brunsing, R.L., Schenker-Ahmed, N.M., White, N.S., Parsons, J.K., Kane, C., Kuperman, J., Bartsch, H., Kader, A.K., Rakow-Penner, R., Seibert, T.M., Margolis, D., Raman, S.S., McDonald, C.R., Farid, N., Kesari, S., Hansel, D., Shabaik, A., Dale, A.M., Karow, D.S., 2017. Restriction spectrum imaging: An evolving imaging biomarker in prostate MRI. J. Magn. Reson. Imaging 45 (2), 323–336.

Chung, S., Lu, Y., Henry, R.G., 2006. Comparison of bootstrap approaches for estimation of uncertainties of DTI parameters. Neuroimage 33 (2), 531–541.

Conlin, C.C., Feng, C.H., Rodriguez-Soto, A.E., Karunamuni, R.A., Kuperman, J.M., Holland, D., Rakow-Penner, R., Hahn, M.E., Seibert, T.M., Dale, A.M., 2021. Improved characterization of diffusion in normal and cancerous prostate tissue through optimization of multicompartmental signal models. J. Magn. Reson. Imaging 53 (2), 628–639.

Cross, A.H., Song, S.-K., 2017. "A new imaging modality to non-invasively assess multiple sclerosis pathology". J. Neuroimmunol. 304, 81–85.

de Bruijn, C.A.M., Di Michele, S., Tataranno, M.L., Ramenghi, L.A., Rossi, A., Malova, M., Benders, M., van den Hoogen, A., Dudink, J., 2023. Neurodevelopmental consequences of preterm punctate white matter lesions: a systematic review. Pediatr. Res. 93 (6), 1480–1490.

DiPiero, M., Rodrigues, P.G., Gromala, A., Dean, D.C., 2022. Applications of advanced diffusion MRI in early brain development: a comprehensive review. Brain Struct. Funct..

Dubois, J., Alison, M., Counsell, S.J., Hertz-Pannier, L., Hüppi, P.S., Benders, M.J.N.L., 2021. MRI of the neonatal brain: A review of methodological challenges and neuroscientific advances. J. Magn. Reson. Imaging 53 (5), 1318–1343.

Greve, D.N., Fischl, B., 2009. Accurate and robust brain image alignment using boundary-based registration. Neuroimage 48 (1), 63–72.

Guo, T., Duerden, E.G., Adams, E., Chau, V., Branson, H.M., Chakravarty, M.M., Poskitt, K.J., Synnes, A., Grunau, R.E., Miller, S.P., 2017. Quantitative assessment of white matter injury in preterm neonates: Association with outcomes. Neurology 88 (7), 614–622.

Han, R.H., Johanns, T.M., Roberts, K.F., Tao, Y., Luo, J., Ye, Z., Sun, P., Blum, J., Lin, T.-H., Song, S.-K., Kim, A.H., 2023. Diffusion basis spectrum imaging as an adjunct to conventional MRI leads to earlier diagnosis of high-grade glioma tumor progression versus treatment effect. Neurooncol. Adv. 5 (1), vdad050.

Hayman, M., van Wezel-Meijler, G., van Straaten, H., Brilstra, E., Groenendaal, F., de Vries, L.S., 2019. Punctate white-matter lesions in the full-term newborn: Underlying aetiology and outcome. Eur. J. Paediatr. Neurol. 23 (2), 280–287.

Henf, J., Grothe, M.J., Brueggen, K., Teipel, S., Dyrba, M., 2018. Mean diffusivity in cortical gray matter in alzheimer's disease: The importance of partial volume correction. NeuroImage Clin. 17, 579–586.

Isaacs, A.M., Neil, J.J., McAllister, J.P., Dahiya, S., Castaneyra-Ruiz, L., Merisaari, H., Botteron, H.E., Alexopoulous, D., George, A., Peng, S., Morales, D., Yan, Y., Song, S.-K., Limbrick, D.D., Smyser, C.D., 2021. Diffusion basis spectrum imaging in post-hemorrhagic hydrocephalus of prematurity. MedRxiv, 2021.01. 12.21249706.

Jelescu, I.O., Budde, M.D., 2017. Design and validation of diffusion MRI models of white matter. Front. Phys. 28.

Jelescu, I.O., Palombo, M., Bagnato, F., Schilling, K.G., 2020. Challenges for biophysical modeling of microstructure. J. Neurosci. Methods 344 (108861), 108861.

Jenkinson, M., Bannister, P., Brady, M., Smith, S., 2002. Improved optimization for the robust and accurate linear registration and motion correction of brain images. Neuroimage 17 (2), 825–841.

Jeon, T., Fung, M.M., Koch, K.M., Tan, E.T., Sneag, D.B., 2018. Peripheral nerve diffusion tensor imaging: Overview, pitfalls, and future directions. J. Magn. Reson. Imaging 47 (5), 1171–1189.

Kelly, C., Dhollander, T., Harding, I.H., Khan, W., Beare, R., Cheong, J.L., Doyle, L.W., Seal, M., Thompson, D.K., Inder, T.E., Anderson, P.J., 2022. Brain tissue microstructural and free-water composition 13 years after very preterm birth. Neuroimage 254 (119168), 119168.

Kersbergen, K.J., Benders, M.J.N.L., Groenendaal, F., Koopman-Esseboom, C., Nievelstein, R.A.J., van Haastert, I.C., de Vries, L.S., 2014. Different patterns of punctate white matter lesions in serially scanned preterm infants. PLoS ONE 9 (10), e108904.

Kim, E.H., Jing, H., Utt, K.L., Vetter, J.M., Weimholt, R.C., Bullock, A.D., Klim, A.P., Bergeron, K.A., Frankel, J.K., Smith, Z.L., Andriole, G.L., Song, S.-K., Ippolito, J.E., 2025. An artificial intelligence model using diffusion basis spectrum imaging metrics accurately predicts clinically significant prostate cancer. J. Urol. 101097JU0000000000004456.

Kingsley, P.B., 2006. Introduction to diffusion tensor imaging mathematics: Part I. tensors, rotations, and eigenvectors. Concepts Magn. Reson. Part A Bridg. Educ. Res. 28A (2), 101–122.

Le Bihan, D., Mangin, J.F., Poupon, C., Clark, C.A., Pappata, S., Molko, N., Chabriat, H., 2001. Diffusion tensor imaging: concepts and applications. J. Magn. Reson. Imaging 13 (4), 534–546.

Lerch, J.P., van der Kouwe, A.J.W., Raznahan, A., Paus, T., Johansen-Berg, H., Miller, K.L., Smith, S.M., Fischl, B., Sotiropoulos, S.N., 2017. Studying neuroanatomy using MRI. Nat. Neurosci. 20 (3), 314–326.

Lin, T.-H., Sun, P., Hallman, M., Hwang, F.C., Wallendorf, M., Ray, W.Z., Spees, W.M., Song, S.-K., 2019. Noninvasive quantification of axonal loss in the presence of tissue swelling in traumatic spinal cord injury mice. J. Neurotrauma 36 (15), 2308–2315.

Makropoulos, A., Robinson, E.C., Schuh, A., Wright, R., Fitzgibbon, S., Bozek, J., Counsell, S.J., Steinweg, J., Vecchiato, K., Passerat-Palmbach, J., Lenz, G., Mortari, F., Tenev, T., Duff, E.P., Bastiani, M., Cordero-Grande, L., Hughes, E., Tusor, N., Tournier, J.-D., Hutter, J., Price, A.N., Teixeira, R.P.A.G., Murgasova, M., Victor, S., Kelly, C., Rutherford, M.A., Smith, S.M., Edwards, A.D., Hajnal, J.V., Jenkinson, M., Rueckert, D., 2018. The developing human connectome project: A minimal processing pipeline for neonatal cortical surface reconstruction. Neuroimage 173, 88–112.

Merboldt, K.-D., Hanicke, W., Frahm, J., 1985. Self-diffusion NMR imaging using stimulated echoes. J. Magn. Reson. 64 (3), 479–486.

Motta, A., Berning, M., Boergens, K.M., Staffler, B., Beining, M., Loomba, S., Hennig, P., Wissler, H., Helmstaedter, M., 2019. Dense connectomic reconstruction in layer 4 of the somatosensory cortex. Science 366 (6469), eaay3134.

Nanba, Y., Matsui, K., Aida, N., Sato, Y., Toyoshima, K., Kawataki, M., Hoshino, R., Ohyama, M., Itani, Y., Goto, A., Oka, A., 2007. Magnetic resonance imaging regional T1 abnormalities at term accurately predict motor outcome in preterm infants. Pediatrics 120 (1), e10–9.

de Bruïne, F.T., van den Berg-Huysmans, A.A., Leijser, L.M., Rijken, M., Steggerda, S.J., van der Grond, J., van Wezel-Meijler, G., 2011. Clinical implications of MR imaging findings in the white matter in very preterm infants: a 2-year follow-up study. Radiology 261 (3), 899–906.

Nguyen, A.L.A., Ding, Y., Suffren, S., Londono, I., Luck, D., Lodygensky, G.A., 2019. The brain's kryptonite: Overview of punctate white matter lesions in neonates. Int. J. Dev. Neurosci. 77, 77–88.

Niendorf, T., Dijkhuizen, R.M., Norris, D.G., van Lookeren Campagne, M., Nicolay, K., 1996. Biexponential diffusion attenuation in various states of brain tissue: implications for diffusion-weighted imaging. Magn. Reson. Med. 36 (6), 847–857.

Niwa, T., de Vries, L.S., Benders, M.J.N.L., Takahara, T., Nikkels, P.G.J., Groenendaal, F., 2011. Punctate white matter lesions in infants: new insights using susceptibility-weighted imaging. Neuroradiology 53 (9), 669–679.

Palombo, M., Ianus, A., Guerreri, M., Nunes, D., Alexander, D.C., Shemesh, N., Zhang, H., 2020. SANDI: A compartment-based model for non-invasive apparent soma and neurite imaging by diffusion MRI. Neuroimage 215 (116835), 116835.

Pasternak, O., Sochen, N., Gur, Y., Intrator, N., Assaf, Y., 2009. Free water elimination and mapping from diffusion MRI. Magn. Reson. Med. 62 (3), 717–730.

Pavaine, J., Young, J.M., Morgan, B.R., Shroff, M., Raybaud, C., Taylor, M.J., 2016. Diffusion tensor imaging-based assessment of white matter tracts and visual-motor outcomes in very preterm neonates. Neuroradiology 58 (3), 301–310.

Pierpaoli, C., Jezzard, P., Basser, P.J., Barnett, A., Di Chiro, G., 1996. Diffusion tensor MR imaging of the human brain. Radiology 201 (3), 637–648.

Ramirez-Manzanares, A., Rivera, M., Vemuri, B.C., Carney, P., Mareci, T., 2007. Diffusion basis functions decomposition for estimating white matter intravoxel fiber geometry. IEEE Trans. Med. Imaging 26 (8), 1091–1102.

Rodríguez-Soto, A.E., Andreassen, M.M.S., Fang, L.K., Conlin, C.C., Park, H.H., Ahn, G.S., Bartsch, H., Kuperman, J., Vidić, I., Ojeda-Fournier, H., Wallace, A.M., Hahn, M., Seibert, T.M., Jerome, N.P., Østlie, A., Bathen, T.F., Goa, P.a.E., Rakow-Penner, R., Dale, A.M., 2022. Characterization of the diffusion signal of breast tissues using multi-exponential models. Magn. Reson. Med. 87 (4), 1938–1951.

Rutherford, M.A., Supramaniam, V., Ederies, A., Chew, A., Bassi, L., Groppo, M., Anjari, M., Counsell, S., Ramenghi, L.A., 2010. Magnetic resonance imaging of white matter diseases of prematurity. Neuroradiology 52 (6), 505–521.

Song, S.-K., Sun, S.-W., Ramsbottom, M.J., Chang, C., Russell, J., Cross, A.H., 2002. Dysmyelination revealed through MRI as increased radial (but unchanged axial) diffusion of water. Neuroimage 17 (3), 1429–1436.

Sun, S.-W., Liang, H.-F., Trinkaus, K., Cross, A.H., Armstrong, R.C., Song, S.-K., 2006. Noninvasive detection of cuprizone induced axonal damage and demyelination in the mouse corpus callosum. Magn. Reson. Med. 55 (2), 302–308.

Tusor, N., Benders, M.J., Counsell, S.J., Nongena, P., Ederies, M.A., Falconer, S., Chew, A., Gonzalez-Cinca, N., Hajnal, J.V., Gangadharan, S., Chatzi, V., Kersbergen, K.J., Kennea, N., Azzopardi, D.V., Edwards, A.D., 2017. Punctate white matter lesions associated with altered brain development and adverse motor outcome in preterm infants. Sci. Rep. 7 (1), 13250.

Van Jay Wedeen Reese, Tuch, D.S., Weigel, M.R., Dou, J.G., Weiskoff, R.M., Chessler, D., 2000. Wedeen Mapping Fiber Orientation Spectra in Cerebral White Matter with Fourier-Transform Diffusion MRI, vol. 8, p. 82.

Wang, Y., Sun, P., Wang, Q., Trinkaus, K., Schmidt, R.E., Naismith, R.T., Cross, A.H., Song, S.-K., 2015. Differentiation and quantification of inflammation, demyelination and axon injury or loss in multiple sclerosis. Brain 138 (Pt 5), 1223–1238.

Wang, Y., Wang, Q., Haldar, J.P., Yeh, F.-C., Xie, M., Sun, P., Tu, T.-W., Trinkaus, K., Klein, R.S., Cross, A.H., Song, S.-K., 2011. Quantification of increased cellularity during inflammatory demyelination. Brain 134 (Pt 12), 3590–3601.

White, N.S., Leergaard, T.B., D'Arceuil, H., Bjaalie, J.G., Dale, A.M., 2013. Probing tissue microstructure with restriction spectrum imaging: Histological and theoretical validation. Hum. Brain Mapp. 34 (2), 327–346.

Winklewski, P.J., Sabisz, A., Naumczyk, P., Jodzio, K., Szurowska, E., Szarmach, A., 2018. Understanding the physiopathology behind axial and radial diffusivity changes-what do we know? Front. Neurol. 9, 92.

Yablonskiy, D.A., Bretthorst, G.L., Ackerman, J.J.H., 2003. Statistical model for diffusion attenuated MR signal. Magn. Reson. Med. 50 (4), 664–669.

Ye, Z., Price, R.L., Liu, X., Lin, J., Yang, Q., Sun, P., Wu, A.T., Wang, L., Han, R.H., Song, C., Yang, R., Gary, S.E., Mao, D.D., Wallendorf, M., Campian, J.L., Li, J.-S., Dahiya, S., Kim, A.H., Song, S.-K., 2020. Diffusion histology imaging combining diffusion basis spectrum imaging (DBSI) and machine learning improves detection and classification of glioblastoma pathology. Clin. Cancer Res. 26 (20), 5388–5399.

Zhang, J.K., Javeed, S., Greenberg, J.K., Yakdan, S., Kaleem, M.I., Botterbush, K.S., Benedict, B., Dibble, C.F., Sun, P., Sherrod, B., Dailey, A.T., Bisson, E.F., Mahan, M., Mazur, M., Song, S.-K., Ray, W.Z., 2025. Diffusion MRI metrics characterize postoperative clinical outcomes after surgery for cervical spondylotic myelopathy. Neurosurgery 96 (1), 69–77.

Zhang, E., Londono, I., Fouquet, J., Pshezhetsky, A., De Leener, B., Lodygensky, G., 2023. A novel method for detecting neuroinflammation in mouse brain with sanfilippo syndrome. In: ISMRM.

Zhang, H., Schneider, T., Wheeler-Kingshott, C.A., Alexander, D.C., 2012. NODDI: practical in vivo neurite orientation dispersion and density imaging of the human brain. Neuroimage 61 (4), 1000–1016.